Biointerface Research in Applied Chemistry
Open-Access Journal (ISSN: 2069-5837)

Article
Volume 16, Issue 2, 2026, 54
https://doi.org/10.33263/BRIAC162.054

Molecular Docking-Guided Investigation of Antibacterial Activity of PVP-Assisted Surface-Modified Fullerene C_{60} Nanoformulations

Kumari Anamika [1], Manoranjan Behera [1,*], Anshuman Sarangi [2] Ashok Kumar Sarangi [2], Alok Ranjan Nayak [2]

[1] Department of Basic Sciences and Humanities, Silicon University, Odisha, 751024, India
[2] Trident School of Biotechnology, Trident Academy of Creative Technology, Odisha, 751024, India
* Correspondence: manoranjan@silicon.ac.in;

Received: 3.07.2025; Accepted: 6.02.2026; Published: 15.04.2026

Abstract: This study investigates the synthesis and characterization of poly (vinyl pyrrolidone) PVP and C_{60} nanofluids (NFs), analyzing their antibacterial properties against gram-positive and gram-negative bacteria. The synthesized NFs were characterized using techniques such as UV-Visible, Fourier Transform Infrared (FTIR), and Photoluminescence (PL) spectroscopy, Dynamic Light Scattering (DLS), Scanning Electron Microscopy (SEM), and Transmission Electron Microscopy (TEM). Notably, changes in the electronic absorption spectra indicated interactions between PVP and C_{60}, evidenced by a hypsochromic shift in peak positions. FTIR spectra corroborate the existence of weak interactions between PVP and C_{60} molecules. DLS analysis revealed hydrodynamic diameters ranging from 120 nm to 400 nm, increasing with C_{60} concentration. Microscopic studies using SEM and TEM highlighted the morphology of PVP-encapsulated C_{60} clusters, ranging from 30 nm to 150 nm, with aggregation observed at higher C_{60} concentrations. The nanofluids demonstrated antibacterial efficacy, exhibiting zones of inhibition between 4 mm and 10 mm in agar well diffusion assays against gram-negative *Escherichia coli*, *Pseudomonas aeruginosa*, and gram-positive *Staphylococcus aureus*. Molecular docking simulations determined the negative free energy changes -10.3, -12.5, and -11.2 Kcal/mol, which reflect favorable interactions between PVP-coated C_{60} nanoparticles with bacterial outer membrane proteins (OmpX of *Esherichia coli* and OprG of *Pseudomonas aeruginosa*) and membrane stabilizing protein (MspA of *Staphylococcus aureus*). Minimum inhibitory concentration (MIC) and minimum bactericidal concentration (MBC) values were subsequently determined using a Resazurin-based two-fold tube dilution method against. The presence of both MIC and MBC values in each sample validates their effective antibacterial properties.

Keywords: fullerene C_{60}; surface modification; light quenching, antibacterial activity; molecular docking; minimum inhibitory concentration; minimum bactericidal concentration.

1. Introduction

Fullerene C_{60}, named as buckminsterfullerene, a unique cluster of sixty carbon atoms and resembling the shape of a soccer ball, has wide applications in the field of medicine, cosmetics, electronics, water treatment, corrosion prevention, photovoltaics, photo detectors, and many more. In order to provide a stable structure, this wonder carbon cluster consists of

12 pentagons and 20 hexagons, wherein no two pentagons are adjacent to each other as per the isolated pentagon rule. Due to the development of strain in the cluster, the carbon atom is not strictly sp^2 but has some sp^3 character owing to the curvature of the molecular surface [1, 2]. The existence of local strain in each carbon atom in the closed-cage structure is the main driving force for the execution of many chemical reactions by the C_{60} molecule. As an electron acceptor with an electron affinity of 2.65 eV, it can accept up to six electrons from an electron donor molecule and has radical scavenging capacity [3].

Despite the possession of many good properties, the very poor solubility or almost insolubility of C_{60} in water restricts its application in biomedical fields [4]. As per the report by Ruoff *et al*. [5], the solubility of C_{60} in organic solvents lies below 52 mg/mL. The solubility of C_{60} relies on the "like dissolves like" principle. It is high if the solvent has a large refractive index, at least a dielectric constant of 4, a large molecular volume, ability to form H-bonding, existence of π-π interaction, has a tendency to act as a moderate nucleophile, and Hildebrand solubility parameter equal to 10 $cal^{1/2}\,cm^{-3/2}$. The solubility of C_{60} in 1-chloronaphthalene is 51 mg/mL due to a high refractive index of 1.63, dielectric constant of 5, and molecular volume of 136 $cm^3\,mol^{-1}$ and Hildebrand solubility parameter of 9.8 $cal^{1/2}\,cm^{-3/2}$ [5].

Though the solubility of C_{60} in water is very poor, solubilization can be increased through the four routes such as (1) surface functionalization by attaching hydrophilic functional group on the surface of C_{60}, (2) solvent exchange, (3) long-term stirring/sonication of C_{60} powder in water, and (4) surface modification using stabilizing agents like surfactants, polymers, cyclodextrin, etc. Absorption spectrum of Poly(N-vinyl-pyrrolidone-alt-maleic anhydride) capped C_{60} solution shows broad bands near 260 and 340 nm. The bands were ascribed to clustering of C_{60} in the aqueous medium and its complexation with the copolymer and solvent molecules [6]. The hydrodynamic diameter of polymer-capped C_{60} particles in the aqueous medium is reported to lie between 116 and 200 nm, with a polydispersity index of 0.20-0.40. The zetapotential measured for the samples was reported to be between -16.0 and -20.0 mV, contributing to good colloidal stability in an aqueous medium. The negative charge on the surface of the C_{60} molecule results from the accumulation of electrons originating from the electron donor atoms of the copolymer. The overlapping of C_{60} and polymer bands in the FTIR spectrum suggests the formation of a C_{60}-polymer complex in the medium. Fullerene molecules solubilized by crosslinking with a supramolecular polymer exhibit hydroxyl radical scavenging property even at a low dose. The dynamic light scattering study of the C_{60}-polymer nanofluids suggests an increase in the particle size from 170 nm to 345 nm when C_{60} molecules were encapsulated in the micelle formed by the polymer.

Huang *et al*. and Grodniski *et al*. [7,8]studied the photoluminescence quenching ability of C_{60} molecules and stated that the photoluminescence of semiconducting polymer nanoparticles decreases, while the photothermal effect increases with a rise in the C_{60} concentration. This is attributed to the enhanced non-radiative recombination of charge transfer excitons. The thermal and rheological properties of Polyurethane (PU)-C_{60} nanocomposite were studied, and it was stated that these two properties depend on the type of isocyanates and C_{60} loading in the composites. Agglomerated morphology seen in the PU-C_{60} nanocomposite is ascribed to the strong van der Waals forces of attraction and extensive π-π stacking interactions [9]. They studied the vibrational spectra of the composite to suggest interactions between C_{60} and polymer matrix, as some of the vibrational bands, such as C-H, N-H, and C=O stretching of the polymer, undergo variations in peak position and height. The non-Newtonian signature reported for the composite is due to the formation of a three-dimensional network

structure between C_{60} and the polymer molecules. Liu *et al*. [10] have synthesized water-soluble C_{60} by complexation with sugar-functionalized tribenzotriquinacene and studied their stability using photoluminescence and Raman spectroscopy. They reported that the complexation between C_{60} and sugar molecules is due to a hydrophobic π-π interaction, resulting in the formation of large agglomerates ranging in size between 300 and 350 nm.

An antibacterial study was done by Samoilova *et al*. [6] for the C_{60} nanofluids solubilized using a copolymer of PVP and maleic acid. They have reported that the prepared nanofluids do not exhibit any antibacterial and antifungal activity against the micro-organisms like *S. aureus*, *P. aeruginosa*, *E. faecalis*, and *C. albicans*, even up to the high PVP-C_{60} concentration of 400 μg/mL C_{60}. In another article by Aoshima *et al*., it is reported that PVP-C_{60} does not exhibit antibacterial activity against any widely studied microorganisms. They further reported that the functionalization of the C_{60} molecule with the –OH group results in fullerenols that exhibit antibacterial activity against many microorganisms. The antibacterial and antifungal activity of the ternary complex containing C_{60}, PVP, and nanodiamond (ND), studied at a concentration of 175 μg/mL of C_{60}, has the ability to effectively inhibit the biofilm formation in *S. aureus* and *E. coli*, and *Candida* microorganisms [11]. They further compared the antibacterial activity with the binary system of PVP + C_{60} and PVP + ND. According to their report, all complexes prevented the formation of bacterial biofilm, but their efficacy depends on several factors, such as the type of microorganism, the composition of nano systems, the dosage, and the exposure time. Targeted drug delivery to the tumor cells, antioxidant and prooxidant activity of a ternary complex containing C_{60}, PVP, and folic acid were studied [12]. It is reported that the complex containing 200 μg/mL C_{60} is non-toxic in vitro and does not affect the cell cycle [12]. In this article, they stated that C_{60} binds to PVP molecules by forming a charge transfer complex, as the C=O band in the FTIR spectrum shifts slightly in the presence of C_{60} molecules [13]. Nanoparticles kill bacteria in a liquid medium by forming singlet oxygen and superoxide. It is reported that C_{60} encapsulated with PVP is more efficient than fullerol in forming singlet oxygen and superoxide [14].

Skariyachan *et al*. and Chaudhary *et al*. [15,16] have mentioned that molecular docking is a powerful computational technique that is used for finding out the possible extent of interactions between the protein or gene with either other proteins or smaller molecules (ligands, which may include nanoparticles). The molecular interactions model provides us with a clear picture of how effectively a nanoparticle can affect the outer membrane proteins or membrane-stabilizing proteins of microorganisms. Our research targeted 3 different proteins, OmpX, OprG, and MspA of *Escherichia coli*, *Pseudomonas aeruginosa*, and *Staphylococcus aureus*, respectively, according to Vogt *et al*. [17]. OmpX is an integral outer membrane protein present in many bacteria, including *Escherichia coli*, that promotes adhesion to and entry into mammalian cells. It also provides protection to the bacterial cell from the human complement system. Similarly, Touw *et al*. and Jurado-Martín *et al*. [18,19] in their articles described OprG as a member of the OmpW family of outer membrane proteins in *Pseudomonas aeruginosa*. It has been proven that it is highly expressed in anaerobic conditions and severely affects the hosts. *Pseudomonas aeruginosa* becomes less cytotoxic towards humans if OprG is absent. Membrane-stabilizing protein MspA present in Staphylococcus aureus contributes to the pathogenicity as it protects the bacteria from the human innate immune system, as quoted in the article of Duggan *et al*. [20].

In this article, we discuss the solubilization of C_{60} via surface modification using poly(vinyl pyrrolidone) PVP as a dispersing and stabilizing agent in water. Both C_{60} and PVP

were solubilized in a common solvent, N-methyl pyrrolidone (NMP), before solubilizing C_{60} in watervia a surface modification route. Molecular docking (i*n silico*) and quantitative analysis of antibacterial properties were done for Gram-positive and Gram-negative microorganisms using the synthesized samples mentioned earlier in the article.

2. Materials and Methods

2.1. Chemicals.

Poly (vinyl pyrrolidone) PVP of weight average molecular weight M_w ~28,000 with degree of polymerization n = 252 (i.e., PVP K25) and highly pure (99.99%) spectroscopic grade C_{60} powder were purchased from Sigma-Aldrich chemicals and Alfa Aesar, respectively, for the preparation of PVP and C_{60} solution. Both PVP and C_{60} were dissolved in a non-aqueous solvent, NMP, purchased from Sigma-Aldrich chemicals.

2.2. Preparation of PVP and C_{60} solution.

1.07 (1.1 mM) PVP solution was prepared by dissolving 3.0 g of PVP in 100 mL of NMP by stirring in a beaker covered with a watch glass on a hot magnetic stirrer maintained at 50−60°C for 2.5 h. After 2.5 h, the sample was cooled and used at room temperature (RT) for synthesizing PVP-C_{60} nanofluids in water. In order to solubilize C_{60} and prepare a 10.0 mL stock solution of 972 µM C_{60}, 7.0 mg of C_{60} was dissolved in 10.0 mL of NMP by stirring in a beaker covered with a watch glass on a magnetic stirrer for 1 h at RT.

2.3. Synthesis of PVP-C_{60} nanofluids in water.

Initially, 5 mL of PVP solution in NMP was taken in a 50 mL beaker and placed on the pan of the magnetic stirrer maintained at RT. Under stirring conditions, 1 mL of C_{60} in NMP was added drop by drop using a micropipette. The mixture was stirred at 700 rpm for 20 minutes at RT. After 20 minutes of stirring, the temperature of the medium was raised to 110°C to evaporate and obtain a dried sample. The dried sample is then kept in an oven fitted with a vacuum pump for 24 h to remove the N-methyl Pyrrolidone completely, as it is toxic for the living cells [21]. Subsequently, the sample was placed on the magnetic stirrer pan, and 5 mL of deionized water was added and stirred for 1 h to dissolve the dried PVP-C_{60} nanocomposite, forming surface-modified C_{60} nanofluids in water. Following the same procedure, we synthesized a total of four samples (sample-1 to sample-4) containing different concentrations of C_{60}. The samples were preserved in a desiccator for later characterization. Figure 1 shows photographs of prepared PVP solution, C_{60} solution in NMP, and C_{60}-PVP nanofluids in water, and Table 1 shows the concentration of C_{60} in mM and mg/ml.

Figure 1. Photographs of samples: PVP, C_{60}, C_{60}-PVP Nanofluids (P1, P2, P3 and P4).

Table 1. C_{60}-PVP Nanofluids (P1, P2, P3 and P4).

C60-PVP nanofluids	Volume of solvent (Fixed) in mL	Volume of 972µM C_{60} in mL	Concentration of C_{60} in mM	Amount of C_{60} in mg/mL
P1	5	1.0	0.19	0.14
P2	5	1.5	0.29	0.21
P3	5	2.0	0.39	0.28
P4	5	2.5	0.49	0.35

2.4. Characterization techniques.

The optical absorption spectra of synthesized aqueous PVP-C_{60} NFs were studied in the 200-900 nm regions of electromagnetic radiation using a Perkin-Elmer Lambda 1050 UV-Visible spectrophotometer. The samples were placed in a quartz cuvette with a 10 mm optical path length, and the spectra were recorded and analyzed against a PVP reference in water. We also studied emission spectra of the synthesized PVP-C_{60} NFs in water using a Perkin Elmer (Model-LS 55) luminescence spectrometer. The emission bands were analyzed by exciting the samples at 300 nm. The Fourier Transform Infrared Spectroscopy (FTIR) was used to obtain spectra in the range 400 to 4000 cm^{-1} vibrational frequency for all the samples. A Thermo Nicolet Corporation FTIR Spectrometer (Model NEXUS-870) was used to extract the data from the liquid samples in attenuated total reflectance (ATR) mode. We used Field Emission Scanning Electron Microscope (FESEM) as well as high-resolution Transmission Electron Microscope (HRTEM) techniques to examine the size, shapes, and distributions of surface-modified C_{60} clusters. For HRTEM, the sample was prepared using the drop-casting method. A small drop of nanofluid was placed on a carbon-coated copper grid and then placed in a vacuum to remove moisture from the sample before measurements. A Dynamic Light Scattering experiment was conducted to determine the hydrodynamic diameter, polydispersity index, and number distributions for the PVP solutions and PVP-C_{60} nanofluids in water using a Malvern Nano Zeta sizer Nano ZS instrument. The same instrument was used to measure zeta potential and surface conductivity of samples in water.

2.5. Antibacterial property assessment.

We studied the antibacterial activity of the four PVP-C_{60} nanofluids containing different concentrations of C_{60} against both gram-positive (*S. aureus*) and gram-negative (*Escherichia coli& Pseudomonas aeruginosa*) bacteria using the agar well diffusion method, which is commonly employed for this purpose for its applicability as an antibiotic [22]. 1 mL of inoculum was spread on the Mueller-Hinton agar plate, and wells were created to hold 50µL of each sample. Control and samples were added to the wells in the plate and incubated at 35°C for 24 Hrs. Azithromycin was used as the positive control antibiotic.

2.6. Molecular docking- in silico study of antibacterial activity of nanofluids.

The outer membrane protein X (OmpX, 171 amino acids) protein structure with PDB ID [1QJ8 (1.90 A)] was obtained from the PDB database [23, 24]. The other two protein structures (OprG, 232 amino acids, and MspA, 105 amino acids) were developed using the Modeler Tool, as it was developed by Rosignoli *et al*. and Web *et al*. [25,26], and validated in Ramachandran Plots and plot statistics, as mentioned by Linhares *et al*. [27]. These proteins have UniProt entry IDs (A0A9Q9JWM8) and (Q2FVZ6), respectively. The active sites of the ompX, oprG, and mspA proteins were predicted using the CastpFold server [28, 29]. The structures of the target ligand molecules, PVP and C_{60}, were obtained from the PubChem

database and conjugated using the Schrodinger suite to form PVP-C_{60} [28, 29]. In the ligand preparation forum, the energy was minimized to fully stabilize the ligand by adding a hydrogen bond [30, 31]. Azithromycin was used (PubChem CID-447043) to compare the free energy changes with the nanofluids due to molecular interactions [32]. The specialized tool, AutoDock 4.2, was employed to perform molecular docking [33]. Initially, each selected protein was prepared by applying the Kolman charge, Gasteiger partial charge, and hydrogen bond [34]. The protein files were then converted to a .pdbqt file, and the ligand (PVP-C_{60}) was also converted to a .pdbqt file for each docking [35]. Next, grid box coordinates were set according to the predetermined binding sites of each protein [36]. The grid box was prepared according to the predicted binding sites. Table 2 represents the detected grid box values for ompX protein are X-dimension: 40, y-dimension: 52, and y-dimension: 84 with x-center: 50.32, y-center: -13.052, and z-center: 52.4; grid values for oprG protein are X-dimension: 58, y-dimension: 54, and y-dimension: 62 with x-center: 8.934, y-center: 19.814 and z-center: 56.471; and the grid values for mspA protein are X-dimension: 46, y-dimension: 50, and y-dimension: 44 with x-center: -13.305, y-center: 2.842 and z-center: 0.44.

Table 2. Grid box values for OmpX, OprG, and MspA proteins.

Protein	X-dimension	Y-dimension	Z-dimension	X-center	Y-center	Z-center
OmpX	40	52	84	50.32	-13.052	52.4
OprG	58	54	62	8.934	19.814	56.471
MspA	46	50	44	-13.305	2.842	0.44

Subsequently, standard docking steps were followed for the molecular docking study [33, 36]. In the molecular docking study, the best docking scores with an RMSD value of 0.0 were taken to ensure the most optimized interaction [37-39]. After performing molecular docking, the protein-ligand complexes were generated and visualized in the ChimeraX tool [40, 41]. For comparative study, Azithromycin (PubChem CID- 447043) was included, and the same docking steps and grid coordinates were followed to obtain the results.

2.7. Quantitative study of antibacterial activity of nanofluids.

To verify *in silico* studies on the antibacterial activity of the nanofluids, the antibacterial activity of the surface-modified C_{60} nanofluids was assessed using the Resazurin-based two-fold dilution MIC Assay Protocol, which was followed to perform quantitative analysis of each sample's effectiveness on bacteria [42, 43]. MBC was also calculated by the extended incubation method. No agar plating was done [44]. Briefly, to perform a MIC assay, a pure culture of the tested bacterial strain is standardized to 5×10^5 colony-forming units (CFU)/mL and exposed to a range of antibiotic concentrations at 37°C for 24 Hrs. After this incubation period, bacterial growth is assessed by observing the turbidity and color intensity of the media at each antibiotic concentration, and the MIC is defined as the lowest concentration of the antimicrobial molecule required to inhibit visible growth of the tested strain. Dark blue or purple indicates no bacterial growth (strong inhibition), pink represents moderate or no inhibition (growth present), and no color shows the color of the control or minimum activity. The MBC was identified as the lowest concentration at which the broth remained clear and showed no turbidity even after 48 hours of incubation, indicating that the bacteria had been killed rather than merely inhibited [44].

3. Results and Discussion

3.1. UV-Visible and FTIR absorption spectra of polymer-modified C_{60} nanofluids.

Figure 2 shows the electronic absorption spectra of C_{60}-PVP nanofluids consisting of (a) 0, (b) 0.19, (c) 0.29, (d) 0.39, and (e) 0.49 mM C_{60}. In the spectra, 'a' represents the absorption spectrum of C_{60} solution, displaying three characteristic C_{60} bands at 294 nm, 338 nm, and 433 nm in water medium. The absorption spectrum of PVP (Figure 2b) in water gives two bands, one at 297 nm and the other at 350 nm. The band at 297 nm is due to n $\rightarrow\pi^*$ (C=O group of pyrrolidone molecule) transition, and the band at 350 nm arises due to the formation of a complex between PVP and water molecules [20, 21]. From Figure 2, it is observed that when C_{60} molecules are added to the PVP solution to form C_{60}-PVP nanofluids, the absorption spectra exhibit a different signature than those of the individual C_{60} and PVP molecules. By comparing the absorption spectrum of C_{60} (Figure 2a) and a C_{60}-PVP nanofluid containing 4.52 mM of C_{60} (Figure 2c), it is observed that the band at 294 nm of C_{60} has blue-shifted to 291 nm and the band at 338 nm of C_{60} has blue-shifted to 318 nm. This hypsochromic/blue shift in the bands suggests a change in the dielectric medium due to surface modification of C_{60} molecules by PVP molecules through the formation of a donor (PVP molecule)-acceptor (C_{60} molecule) complex.

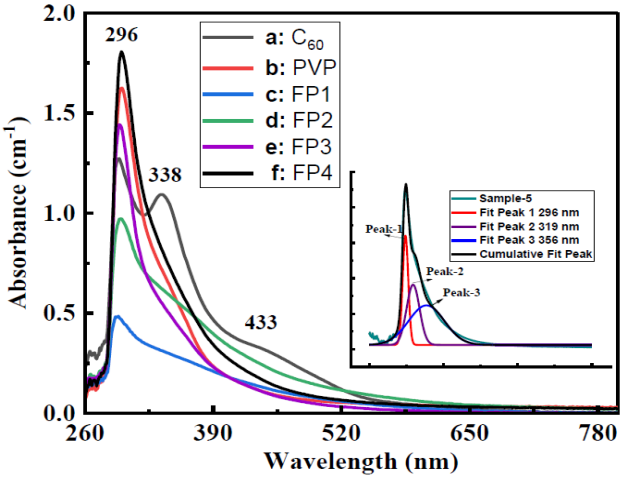

Figure 2. Electronic absorption spectra of C_{60}-PVP nanofluids consisting of **(a)** 0; **(b)** 0.19; **(c)** 0.29; **(d)** 0.39; **(e)** 0.49 mM C_{60}.

Additionally, comparing the band at 296 nm of the PVP solution with a band at 356 nm for a C_{60}-PVP nanofluid containing 0.49 mM of C_{60} shows a slight redshift, indicating the formation of a PVP-water complex. The inset of Figure 1 displays a deconvoluted spectrum for a C_{60}-PVP nanofluid containing 0.19 mM C_{60}, revealing three peaks at 296 nm, 318 nm, and 356 nm. Similar deconvolution can also be applied to other samples to identify these three bands. The absorption spectra also show a redshift in these bands as the C_{60} content in the nanofluids increases. This result suggests that the interaction between C_{60} and PVP molecules slightly decreases with an increase in the C_{60} content and a decrease in the number of capping molecules available per C_{60} molecule in the system. This behavior observed between these parameters indicates a donor-acceptor type interaction between PVP and C_{60} molecules [45].

We studied the FTIR bands in the spectra of various samples to determine whether any interactions exist between C_{60} and PVP molecules. Figure 3 shows FTIR spectra of PVP and C_{60}-PVP nanofluids in water. The PVP molecule in water exhibits a broad O-H stretching vibration band at 3400 cm^{-1} from the solvent molecules. The three bands at 2976, 2945, and

2881 $cm^{-1}$are due to C−H stretching, the C=O stretching band at 1677 cm^{-1}, and the amide-I band at 1651 cm^{-1} are from the pyrrolidone group of PVP. We also observed C–N stretching bands at 1502 and 1430 cm^{-1}, C–H_2 wagging at 1296 cm^{-1}, C-N bending at 1265 cm^{-1}, CH_2 rocking at 1025 cm^{-1}, and CH_2 bending bands at 847 cm^{-1} [46]. A modified FTIR spectrum was noticed for the C_{60}-PVP nanofluid when C_{60} molecules were present along with the PVP molecules in the aqueous medium.

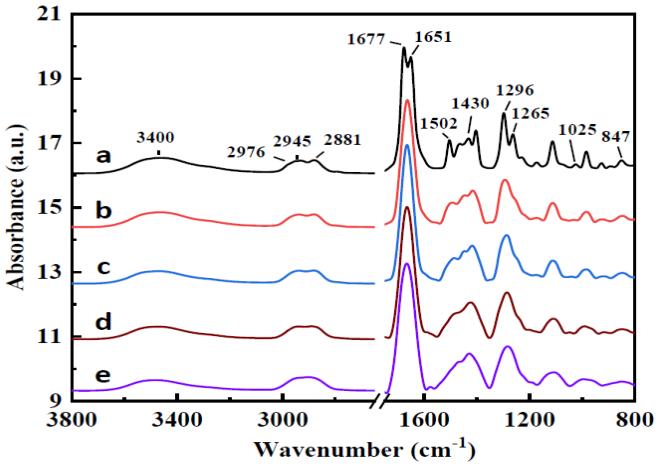

Figure 3. FTIR spectra of PVP-C_{60} nanofluids consisting of **(a)** 0; **(b)** 0.19; **(c)** 0.29; **(d)** 0.39; **(e)** 0.49 mM C_{60}.

The various FTIR bands observed for the PVP molecule and PVP-C_{60} complex are listed in Table 3. The introduction of 0.19 mM C_{60} molecules into the PVP solution results in shifts in some characteristic vibrational bands and a decrease in their intensities.

Table 3. Vibrational band assignment in PVP and PVP-C_{60} complex.

Vibrational band of PVP (cm^{-1})	Vibrational band of PVP - 14.58 nM C_{60} (cm^{-1})	Band assignment
3400	3398	O-H stretching
2976	2974	CH_2 Asymmetric stretching of the pyrrole ring
2945	2943	CH_2 Asymmetric stretching of the pyrrolidone ring
2881	2878	CH_2 symmetric stretching of the pyrrolidone ring
1677	1662	C=O stretching
1651	-	Amide-1
1502	1495	C-N stretching of the pyrrolidone ring
1432	1428	C-N stretching of the pyrrolidone ring
1296	1292	CH_2 wagging
1266	1261	C-N bending of the pyrrolidone ring
1025	1021	CH_2 rocking
847	843	CH_2 bending

The adjustments in the band features, including shifts in band position and changes in intensity, suggest interaction between C_{60} and PVP molecules in the nanofluids. Major modifications in the band features were observed in the range of 1700 cm^{-1} to 800 cm^{-1}. Upon loading of C_{60}, a slight change in the C-H stretching mode of the PVP molecule was observed in the spectra. The C=O stretching band at 1677 cm^{-1} and amide-I band at 1651 cm^{-1} of the pyrrolidone group of PVP merged into a single band at 1663 cm^{-1}. This significant change in the band features suggests that the pyrrolidone group is involved in encapsulating the C_{60} molecules. Other bands, such as C–N stretching, C–H_2 wagging, C-N bending, and CH_2 rocking of PVP molecules, were also modified in the presence of C_{60} molecules. These bands were altered either in terms of their position, intensity, or both [47].

3.2. Photoluminescence spectra of polymer-modified C_{60} nanofluids.

We discuss how the C_{60} molecules affect the light emission intensity of the broad band due to the n→π* transition of the PVP molecules in terms of emission spectra of PVP-C_{60} nanofluids. Figure 4 shows the light emission spectra of C_{60} molecules, PVP molecules, and the PVP-C_{60} complex. As seen from the plot, the emission spectrum of C_{60} solution shows a band at 443 nm, and PVP molecules exhibit light emission in the n → π* band at 483 nm. When C_{60} is added to the PVP solution, the resulting nanofluids reveal an emission spectrum with a red-shifted band and decreased intensity. For the sample containing 0.19 mM C_{60}, the broad emission band at 489 nm undergoes a red shift of 6 nm and a decrease in the peak intensity by approximately 13%. This red shift indicates the formation of a charge transfer complex between C_{60} and the PVP molecule. Consequently, the light emission of the PVP electron donor molecules decreases upon the addition of C_{60} electron acceptor molecules. Additionally, it was noticed that as the C_{60} content in the nanofluids increases, the extent of band shifting and intensity reduction also increases [48].

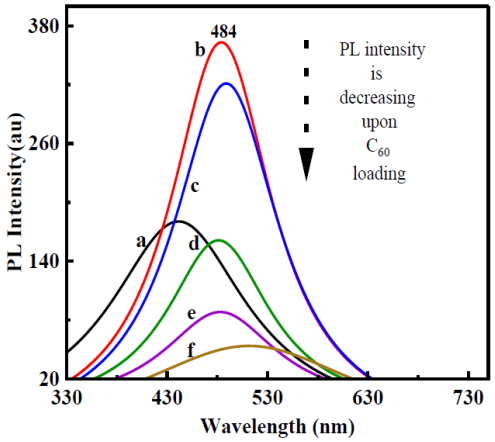

Figure 4. PL spectra of PVP-C_{60} nanofluids consisting of **(a)** C_{60} solution; **(b)** 0; **(c)** 0.19; **(d)** 0.29; **(e)** 0.39; **(f)** 0.49 mM C_{60}.

We also studied the variation of emission band intensity ($I_{int.}$) with C_{60}-contents. As shown in Figure 5, the $I_{int.}$-value decreases with C_{60}-content as charge transfer has occurred from the non-bonding electrons of carbonyl groups of PVP molecules to the vacant highest unoccupied molecular orbitals of C_{60} molecules.

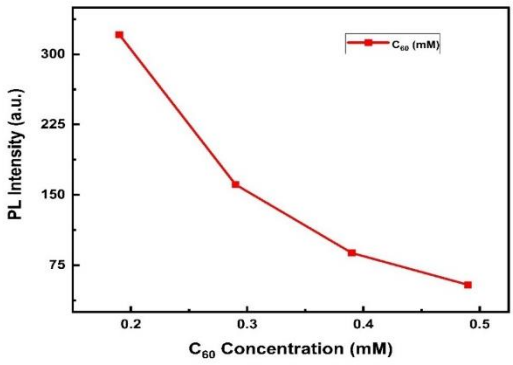

Figure 5. Variation of PL intensity against C_{60} content.

3.3. Dynamic light scattering study.

Nowadays, researchers prefer the Dynamic Light Scattering (DLS) technique to obtain data on the size, distribution, and surface charge of small particles in suspension within a liquid

medium due to its non-destructive nature, speed, efficiency, and high sensitivity. Figure 6 displays the size distributions of particles in C_{60}, PVP, and C_{60}-PVP nanofluids in water. Each sample shows a monomodal distribution of particles with varying width. The width of the band depends on the distribution of C_{60} clusters in the polymer solution. A single DLS band indicates that the clustering of C_{60} particles occurs exclusively through the formation of C_{60}-PVP charge transfer complexes. The average hydrodynamic diameter (D_h) of C_{60} and PVP particles is 110 nm and 200 nm, respectively. For nanofluids, the D_h-value ranges from 120 nm to 400 nm. This result indicates that particle size increases with the C_{60} content, as the number of capping molecules (i.e., PVP) decreases with an increase in C_{60} content in the nanofluids [49].

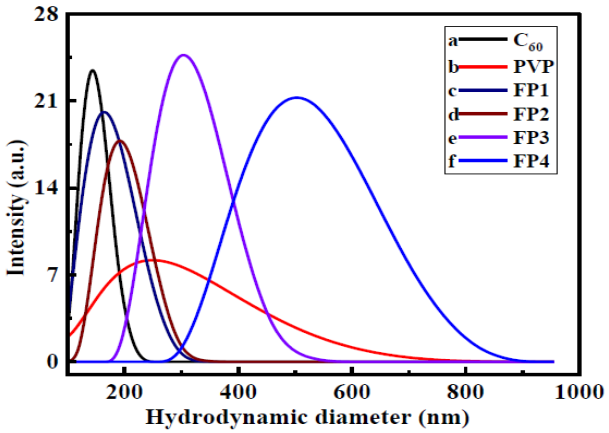

Figure 6. Distribution of D_h-value for **(a)** C_{60}; **(b)** PVP; **(c,d)** PVP-C_{60} nanofluids.

Figure 7 displays the zetapotential distribution for PVP and C_{60}-PVP nanofluids in water.

Similar to the hydrodynamic diameter size distributions, the zetapotential distribution also consists of a single band except for the sample (P4), attributed to clustering through charge transfer (CT) interactions between PVP and C_{60} molecules. For sample P4, two bands are observed, one is attributed to clusters formed via CT interaction, and the other is due to clustering of C_{60} molecules. All the samples exhibit a negative zetapotential band with varying positions, heights, and widths [47]. The full width at half maximum for the zetapotential band of the sample P4 is also relatively higher than that of the other samples. This may be due to the lower number of PVP molecules available per C_{60} molecule in this sample.

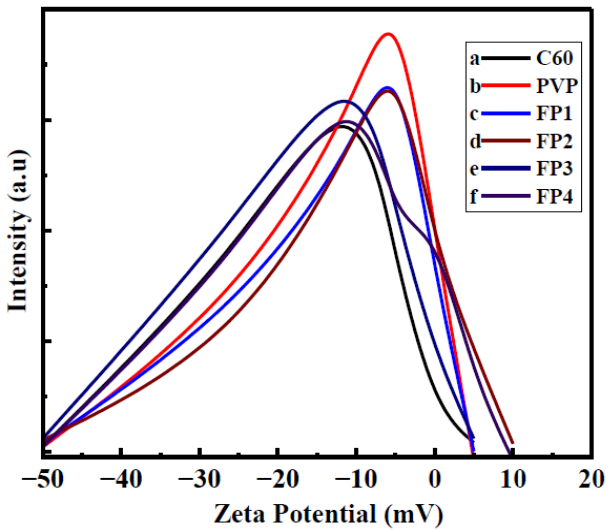

Figure 7. Zetapotential distributions in C_{60}, PVP, and PVP-C_{60} nanofluids.

3.4. Microstructural study.

We used a Scanning Electron Microscope (SEM) and Transmission Electron Microscope (TEM), two powerful imaging techniques, to obtain detailed information about the structure and morphology of materials at the nano-scale. SEM images provide information about topology, while TEM images reveal the internal structure of the sample. Figure 8 shows the SEM images of three samples, P1, P3, and P4. SEM images show PVP-encapsulated C_{60} clusters with sizes ranging between 50 and 150 nm. As the C_{60} content in the sample increases from sample P1 to P4, the number of PVP molecules available to encapsulate each C_{60} molecule decreases. This results in an increase in the PVP-C_{60} cluster size with the increase in C_{60} content. Huang *et al*. [7] have reported polymer-C_{60} clusters with a diameter ranging between 150 and 350 nm. Liu *et al*. [10] reported well-dispersed microspheres with sizes ranging between 0.3 and 0.5 μm for the host-guest C_{60} complex. It has been reported that a mixture of C_{60} and C_{70}, without any encapsulating agent, shows an SEM image with rod-shaped fullerite, with a length in the micrometer range but a width in the nanometer range. This result clearly suggests the role of the encapsulating agent in controlling the dispersion and size of C_{60} clusters [9].

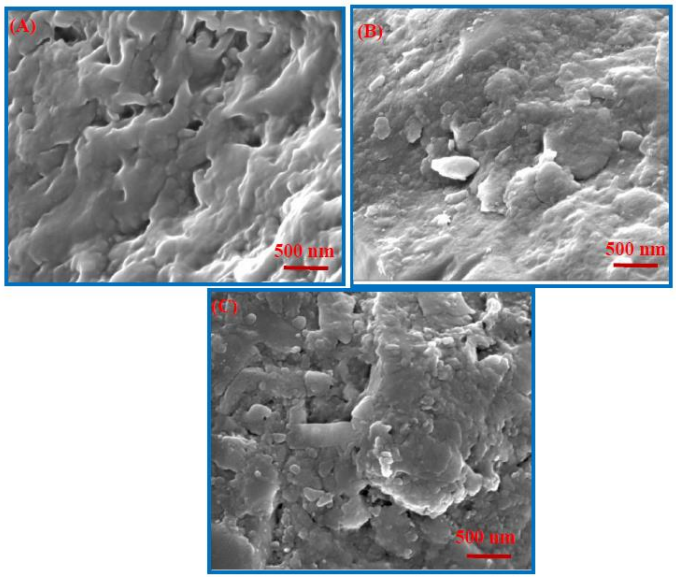

Figure 8. SEM images of PVP-C_{60} composite **(A)** P1; **(B)** P3; **(C)** P4.

Figure 9 shows the TEM images of the same three samples used for SEM imaging. Tong *et al*. [48] reported that C_{60}-PVP complexes form relatively smaller particles, with sizes around 90 nm, compared to C_{60}-Polyoxaxoline (PO) particles, which range from 130 to 150 nm. This statement suggests that the PVP polymer has relatively higher encapsulating power compared to PO. As observed from the TEM image for the sample P1, the sizes of polymer-capped C_{60} clusters range between 30 and 60 nm and are nearly uniform in distribution. With an increase in the C_{60} content in Sample-P3, the cluster size has increased to 70 nm, and coalescence of these clusters is observed. In Sample P4, where the relative number of PVP molecules is lower, clustering appears to grow along a line. A magnified image in Sample P3 (see insert of B) displays C_{60} clusters approximately 5-10 nm in size, crosslinked via PVP molecules. Eom *et al*. [49] reported that C_{60} molecules are solubilized in an aqueous medium by crosslinking with PVP molecules. TEM images of our samples also reveal crosslinking of C_{60} molecules mediated by PVP molecules.

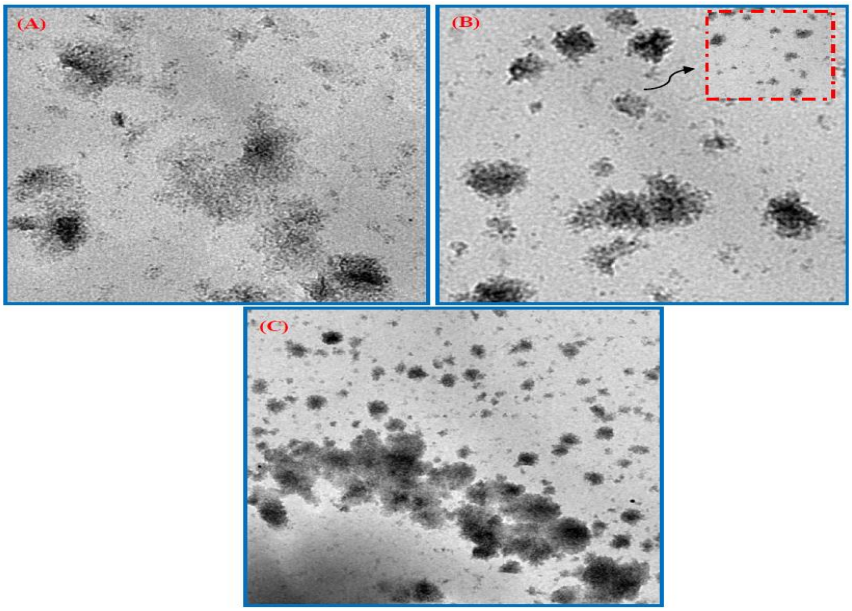

Figure 9. TEM images of PVP-C_{60} composite **(A)** P1; **(B)** P3; **(C)** P4.

3.5. Antibacterial study.

Figure 10 and Table 4 show the zone of inhibition (ZOI) against three selected bacteria. From the image and table, it is concluded that all the samples exhibited antibacterial activity against the bacteria under study, with greater activity observed against the *S. aureus*. Our findings also suggest that the antibacterial activity of aqueous C_{60} is comparable to or less than that of the PVP-C_{60} nanofluids, which is contradictory to the proposed idea. Figures 10 and 11 clearly showed that the nanofluids did not show better antibacterial potential than the control. It might have occurred because of the nanoparticles' lower diffusion capacity. A larger nanoparticle size may be the reason for reduced diffusion in the solid media. The activity of NPs against bacteria is reported to be influenced by various factors, including NP size and shape, roughness, dispersity, surface charge, medium temperature, pH, and osmotic pressure [50]. Additionally, it is influenced by the type of microorganism, the composition of nano systems, the dosage, and the exposure time. Since many parameters determine efficacy, we believe that extensive research on this system is needed to enhance its activity against microorganisms to be on par with that of commonly used antibiotics. To validate our findings, we did an in silico study, which is molecular docking. Also, quantitative analyses were performed by calculating MIC and MBC using the Resazurin-based two-fold tube dilution method for the nanofluids against gram-negative *Escherichia coli*, *Pseudomonas aeruginosa*, and gram-positive *Staphylococcus aureus.*

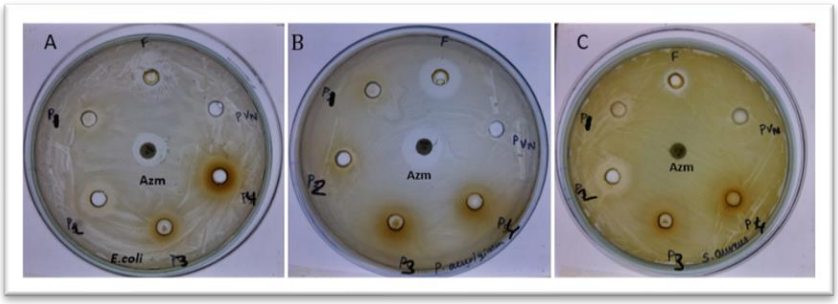

Figure 10. Antibacterial activity assessment by agar well diffusion method of control azithromycine, fullerene (F), PVP (Pvn) & samples P1, P2, P3, and P4 against **(A)** *Escherichia coli*; **(B)** *Pseudomonas aeruginosa*; **(C)** *Staphylococcus aureus.*

Table 4. Zone of inhibition in (mm) with standard deviation (S.D.) of control azithromycine, fullerene in NMP (F), PVP (Pvn), and samples P1, P2, P3, and P4 against **(A)** *Escherichia coli*, **(B)** *Pseudomonas aeruginosa*, **(C)** *Staphylococcus aureus.*

Nanofluids (PVP-C_{60} in mM)	*Escherichia coli*	S.D.	*Pseudomonas aeruginosa*	S.D.	*Staphylococcus aureus*	S.D.
0.19	5	0	4	0	4	0.09
0.29	9	0	6	0	10	0.12
0.39	7	0.16	8	0.15	9	0.25
0.49	10	0.23	10	0.18	9	0.42
Control (Azm)	13	0.23	12	0.21	17	0.51
C_{60}	6	0.05	12	0.04	6	0.06
PVP	0	0	0	0	0	0

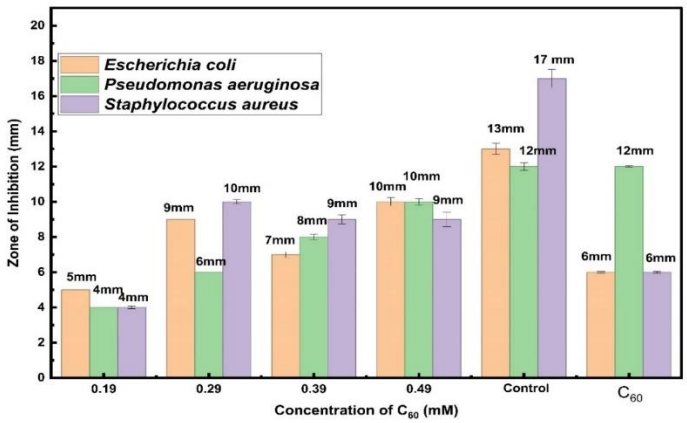

Figure 11. Bar diagram represents zone of inhibition in (mm) with standard deviation (S.D.) of control azithromycine, fullerene in NMP (F), PVP (Pvn), and samples P1, P2, P3, and P4 against **(A)** *Escherichia coli*; **(B)** *Pseudomonas aeruginosa*; **(C)** *Staphylococcus aureus.*

From the above image, table, and figure, it is concluded that all the samples exhibited antibacterial activity against the bacteria under study, with greater activity observed against the *S. aureus*. The analysis also revealed that antibacterial activity increases with the C_{60} content.

The above findings suggest that the PVP-enclosed fullerene interacted with the bacterial cell, thereby disrupting the bacterial biofilm [12]. Our findings indicate that PVP-fullerene nanoparticles in an aqueous medium may be effective at killing bacteria [22, 49]. Surface modification and fabrication are needed to optimize the antibacterial activity of the PVP-fullerene nanofluids [49, 50].

3.6. Molecular docking study

3.6.1. Targeted proteins.

Outer membrane protein X (OmpX) protein structure obtained from the PDB database with PDB id 1QJ8 [15]. The other two structures of proteins (OprG) and (MspA) (Table 5) were developed using the Modeler Tool (Figure 12).

Table 5. Target protein information.

Sl. No.	Entry ID (Uniprot)	Protein name	Gene name	Aminoacid length	PDB ID
1.	P0A917	Outer membrane protein X	ompX	171	1QJ8 (1.90 A^0)
2.	A0A9Q9JWM8	Outer membrane protein OprG	oprG	232	Structure developed
3.	Q2FVZ6	Membrane-stabilizing protein A	mspA	105	Structure developed

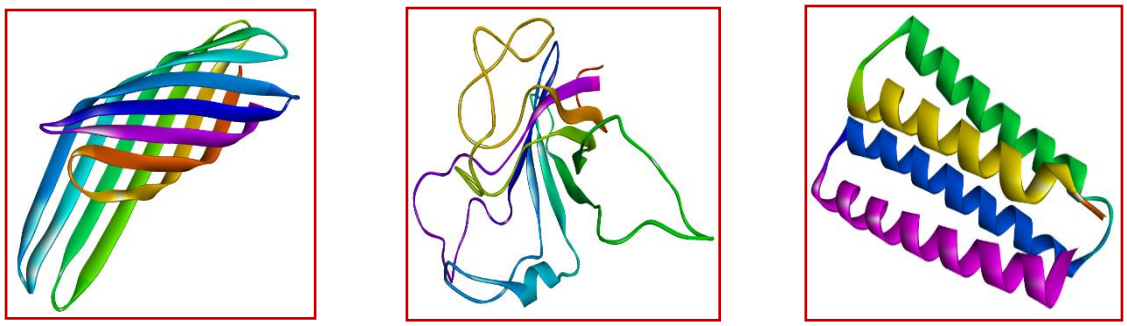

(a) **(b)** **(c)**

Figure 12. 3D-Structure of **(a)** Outer membrane protein X (ompX); **(b)** Outer membrane protein OprG (oprG); **(c)** Membrane-stabilizing protein A (mspA).

3.6.2. Ramachandran plot for protein structural analysis.

The developed structure of oprG and mspA was validated in Ramachandran Plots (Figure 13) and Plot statistics in Tables 6 and 7 [51].

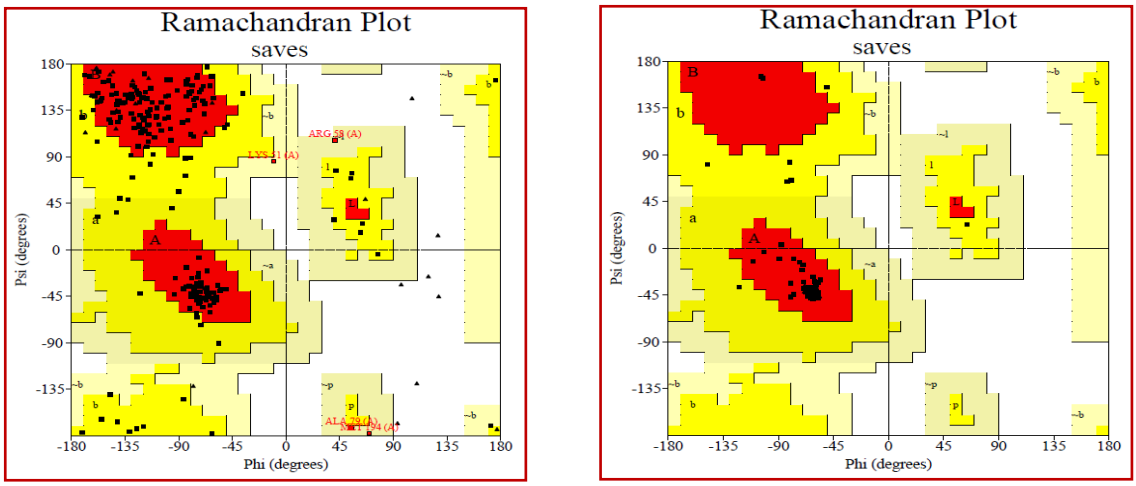

(a) **(b)**

Figure 13. Ramchandran plots of **(a)** Outer membrane protein OprG (oprG); **(b)** Membrane-stabilizing protein A (mspA).

Table 6. The description is based on an analysis of 118 structures of resolution of at least 2.0 Angstroms and R-factor not greater than 20% of the Outer membrane protein OprG.

Sl. No.	Types of residues and regions in the Ramachandran plot	Number of amino acid residues
1	Residues in most favored regions [A, B, L]	146
2	Residues in additional allowed regions [a, b, l, p]	45
3	Residues in generously allowed regions [~a, ~b, ~l, ~p]	4
4	Residues in disallowed regions	0
5	Number of non-glycine and non-proline residues	195
6	Number of end-residues (excluding Gly and Pro)	2
7	Number of glycine residues (shown in triangles)	25
8	Number of proline residues	10
	Total number of residues	232

Table 7. The structure validation of MspA based on an analysis of 118 structures of at least 2.0 Angstroms and R-factor not greater than 20%.

Sl. No.	Types of residues and regions in the Ramachandran plot	Number of amino acid residues
1	Residues in most favored regions [A, B, L]	92
2	Residues in additional allowed regions [a, b, l, p]	06
3	Residues in generously allowed regions [~a, ~b, ~l, ~p]	0
4	Residues in disallowed regions	0
5	Number of non-glycine and non-proline residues	98

Sl. No.	Types of residues and regions in the Ramachandran plot	Number of amino acid residues
6	Number of end-residues (excluding Gly and Pro)	2
7	Number of glycine residues (shown in triangles)	4
8	Number of proline residues	1
	Total number of residues	105

3.6.3. Structure development of the ligand.

The structure of the target ligand molecule PVP (Figure 14a) and C_{60} (Figure 14b) was obtained from the PubChem database and conjugated using the Schrodinger suite to form PVP-C_{60} (Figure 14c).

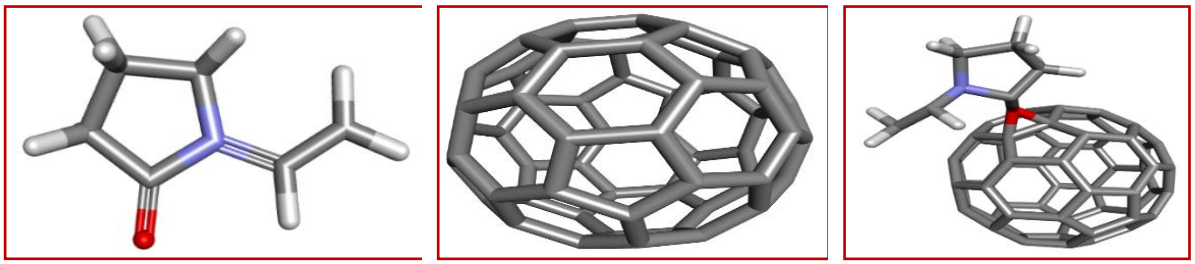

(a) **(b)** **(c)**

Figure 14. 3D-structure of **(a)** PVP; **(b)** C60; **(c)** PVP-C_{60} nanoparticle citation.

3.6.4. Structural analysis of target Proteins OprG and MspA.

Ramachandran plot is a graphical representation used to visualize dihedral angles ϕ and Ψ in protein structures. 90% of the amino acid residues are in the "most favorable regions," which clearly shows the proposed protein conformation is an energetically favorable conformation for amino acid residues in the protein.

3.6.5. Active sites of proteins.

According to the CastpFold server, the active site for ompX protein is Gly16, Gln17, Met18, Asn19, Tyr57, Asn58, Lys59, Asn60, Gln61, Gly88, Lys89, Phe90, Tr92, Ser134, and Val135. For oprG protein active site has Val15, Ala16, Ser17, Phe19, Ala20, Ala21, Asp23, Thr40, Val41, Asp42, Thr68, Gln69, Leu70, Gly71, Thr90, Pro91, Asp167, Ser168, Val191, and Trp192. Active site includes Tyr12, Leu13, Val15, Ser16, Phe17, Ile18, Ser19, Asn67, Val68, Glu69, Val70, and Thr71 for mspA protein.

3.6.6. Molecular docking analysis.

The docking results are analyzed by interaction type and binding affinity.

3.6.6.1. Interaction analysis.

Figures 15 and 16 show the molecular docking results, i.e., interactions between PVP-C_{60} and the active site residues of the proteins. Figure 15 shows the PVP-C_{60} nanoparticles interacting with outer membrane protein X (ompX), outer membrane protein OprG, and membrane-stabilizing protein A (MspA).

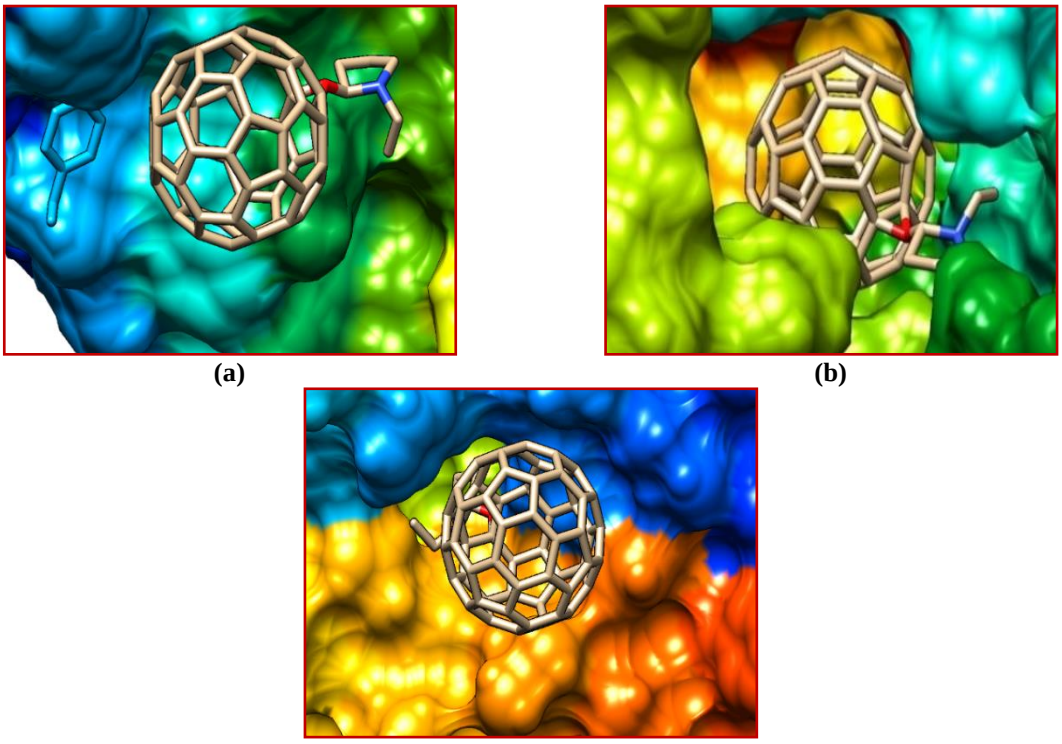

(a) **(b)** **(c)**

Figure 15. Molecular docking 3D-interaction of **(a)** Outer membrane protein X (ompX)-PVP-C_{60}; **(b)** outer membrane protein OprG- PVP-C_{60}; **(c)** Membrane-stabilizing protein A (mspA) - PVP-C_{60} nanoparticle.

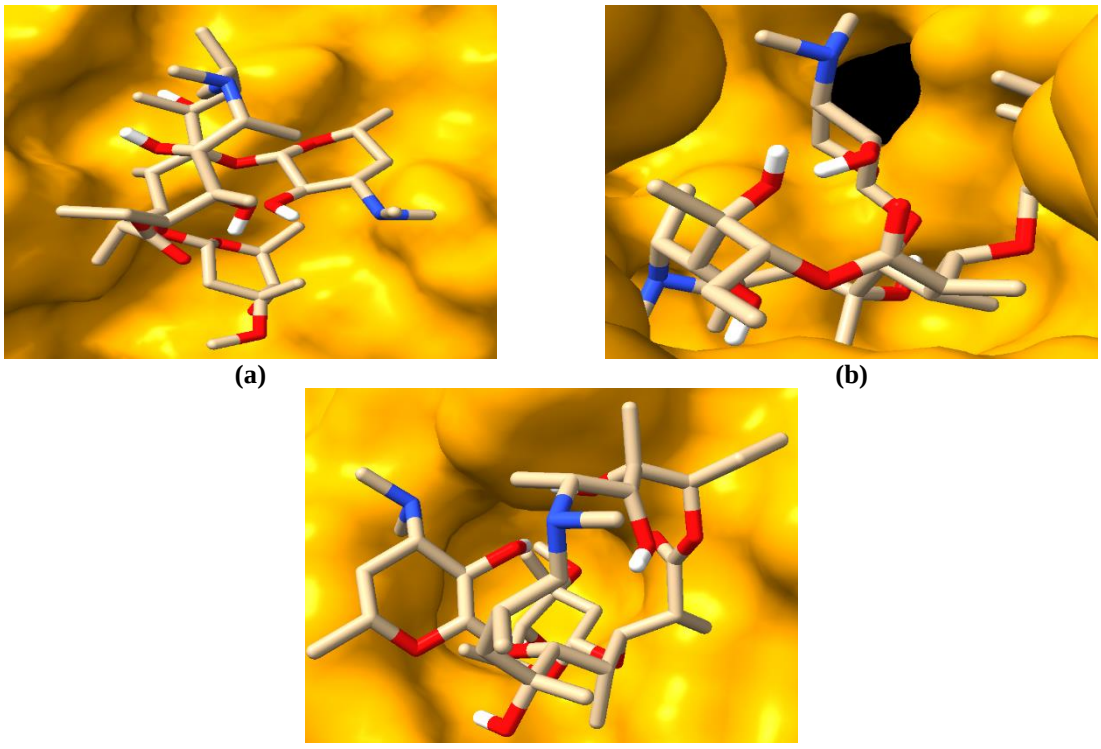

(a) **(b)** **(c)**

Figure 16. Molecular 3D-interaction of **(a)** ompX- Azithromycin; **(b)** oprG- Azithromycin; **(c)** mspA-Azithromycin.

3.6.6.2. Docking affinity.

Table 8 presents the docking results, which indicate that the PVP-C_{60} nanoparticles bind favorably with all three proteins-OmpX, OprG, and MspA-with binding affinities of -10.3 kcal/mol, -12.5 kcal/mol, and -11.2 kcal/mol, respectively, showing the strongest maximum for OprG.

Table 8. Molecular docking simulation results of selected compounds against selected proteins.

Compounds	Docking score (ΔG, kcal/Mol)		
	Outer membrane protein X (ompX)	**Outer membrane protein OprG (oprG)**	**Membrane-stabilizing protein A (mspA)**
PVP-C_{60}	-10.3	-12.5	-11.2
Azithromycin	-06.1	-08.0	-06.3

It was obtained that Azithromycin scored -6.1 kcal/Mol with ompX and -8.0 kcal/Mol with oprG proteins. In the case of the mspA protein, it scored -6.3 kcal/Mol. Remember that all the docking scores have an RMSD value of 0.0.

The favorable binding of PVP-C_{60} nanoparticles to OmpX, OprG, and MspA highlights their potential to disrupt membrane permeability and stability, thereby killing *Escherichia coli*, *Pseudomonas aeruginosa*, and *Staphylococcus aureus* [52]. Here, it is obtained that Azithromycin, the standard ligand, scored lower binding affinities as compared to the PVP-C_{60} nanoparticle. It shows that the PVP-C60 nanoparticle can act more effectively than the marketed compound, Azithromycin, against the targeted proteins. It has been reported that surface modification and fabrication are needed to optimize the antibacterial activity of PVP-C_{60} NFs [53].

3.7. Minimum inhibitory concentration and minimum bactericidal concentration.

Irrespective of nanoparticle size, Figure 17 shows that all synthesized nanofluids exhibited notable antibacterial activity against the tested bacteria. The antimicrobial efficacy, however, differed among the formulations, as reflected by their minimum inhibitory concentration (MIC) and minimum bactericidal concentration (MBC) values. According to the bar graph, 17-nanofluid P3 demonstrated the highest effectiveness against *Escherichia coli*, showing the lowest MIC=4.375 µg/mL and MBC=8.75 µg/mL. In contrast, P2 was most potent against *Pseudomonas aeruginosa*, with the lowest MIC=1.64 µg/mL and MBC=3.28 µg/mL. Meanwhile, P4 exhibited the strongest antibacterial action against *Staphylococcus aureus*, with MIC and MBC values of 2.73 µg/mL and 5.46 µg/mL, respectively [42, 53].

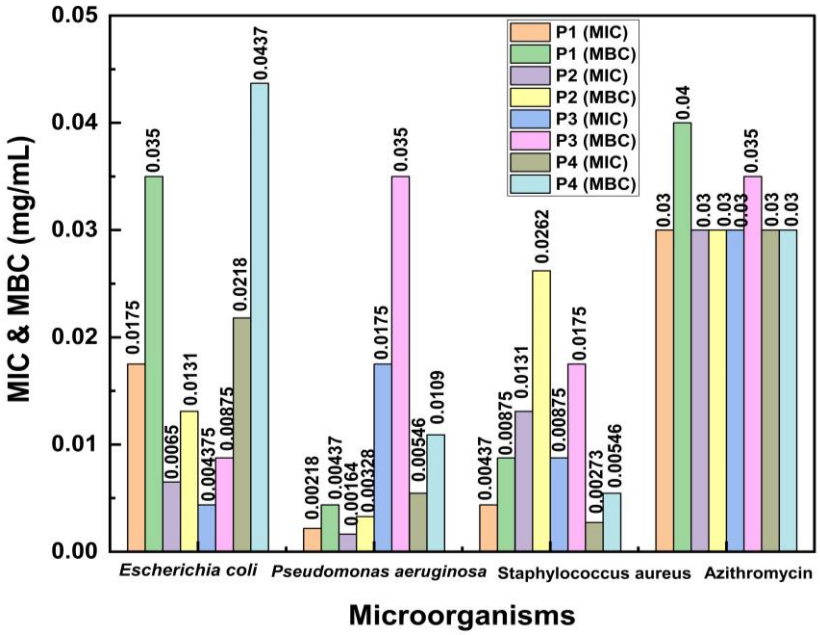

Figure 17. Bar graph representing MIC and MBC values (mg/mL) of P1, P2, P3, and P4 against **(A)** *Escherichia coli*; **(B)** *Pseudomonas aeruginosa*; **(C)** *Staphylococcus aureus*, and the antibiotic Azithromycin.

4. Conclusions

The optical properties of the synthesized nanofluids elucidated essential interactions between PVP and C_{60}, leading to modifications in UV-Visible, FTIR, and PL spectra. FTIR spectra indicated the blue shift in the absorption bands, hinting at the formation of donor-acceptor complexes between PVP and C_{60}. This interaction was further supported by the photoluminescence data, which demonstrated a reduction in emission intensity attributed to the electron transfer process. DLS measurement revealed the hydrodynamic size and polydispersity indices of the NFs, indicating that particle size inversely correlates with the concentration of PVP. This phenomenon emphasizes the importance of capping agents in modulating nanoparticle behavior and stability in aqueous dispersions. All our samples exhibited a negative zetapotential band with varying positions, heights, and widths. The number of PVP molecules available per C_{60} molecule in different samples with different C_{60} concentrations is the main cause. The microstructural studies through TEM showed well-dispersed C_{60} particles encapsulated by PVP molecules under varying concentration conditions. SEM images show PVP-encapsulated C_{60} clusters with sizes ranging between 50 and 150 nm. The PVP-C_{60} NFs exhibited significant antibacterial activity against both gram-positive and gram-negative bacteria, particularly Staphylococcus aureus, with increased C_{60} concentration correlating with enhanced antimicrobial efficacy. Molecular docking studies provided further insight into the mechanisms of action against bacterial targets. The PVP-C_{60} complexes demonstrated favorable binding interactions with membrane-stabilizing and outer membrane proteins, particularly MspA, OmpX, and OprG, which play crucial roles in bacterial survival and virulence. According to the results of a two-fold dilution resazurin-based study, MIC and MBC values are much lower than those of the Azithromycin available in the market, but a few parameters, such as pH, need to be studied and compared. Overall, these results suggest that while all nanofluids are antibacterial, each formulation shows selective efficacy against specific species, but this is not applied in the case of Azithromycin.

Overall, the findings indicate that although all prepared nanofluids exhibit antibacterial activity, each formulation demonstrates selective efficacy against specific bacterial species, unlike Azithromycin, which shows broad-spectrum activity regardless of bacterial type. This selective behavior highlights the potential for tailoring nanofluid formulations for targeted antimicrobial applications. However, the study has certain limitations. The cytotoxic effects of the nanofluids on living cells were not evaluated, which restricts the conclusion regarding their biological safety. In addition, experimental parameter such as pH was not considered, despite their known influence on antimicrobial performance. Such factors may affect the activity and stability of the nanofluids and should be addressed in future studies to provide a more comprehensive assessment of their therapeutic potential.

Author Contributions

Conceptualization, M.B. and A.S.; methodology, M.B.; software, A.S.; validation, M.B., A.S., and K.A.; formal analysis, A.N.; investigation, K.A.; resources, K.A.; data curation, K.A.; writing—original draft preparation, M.B.; writing—review and editing, K.A.; supervision, M.B. All authors have read and agreed to the published version of the manuscript."

Institutional Review Board Statement

Not applicable.

Informed Consent Statement

Not applicable.

Data Availability Statement

Data supporting the findings of this study are available upon reasonable request from the corresponding author.

Funding

This work is funded by Silicon University, Odisha, under the SRPS scheme.

Acknowledgment

We gratefully acknowledge the support from Silicon University, Odisha, and Trident Academy of Creative Technology, Bhubaneswar, India.

Conflict of Interest

There are no conflicts to declare.

References

1. Kausar, A. Breakthroughs of fullerene in optoelectronic devices—An overview. *Hybrid Adv*. **2024**, *6*, 100233, https://doi.org/10.1016/j.hybadv.2024.100233.
2. Rašović, I. Water-soluble fullerenes for medical applications. *Mater. Sci. Technol.* **2016**, *33*, 777–794, https://doi.org/10.1080/02670836.2016.1198114.
3. Huang, D.-L.; Dau, P.D.; Liu, H.-T.; Wang, L.-S. High-resolution photoelectron imaging of cold C_{60}^- anions and accurate determination of the electron affinity of C_{60}. *J. Chem. Phys.* **2014**, *140*, 224315, https://doi.org/10.1063/1.4881421.
4. Wang, D.; Zhao, J.; Mulder, R.J.; Ratcliffe, J.; Wang, C.; Wu, B.; Wang, J.; Hao, X. Highly aqueously stable C_{60}-polymer nanoparticles with excellent photodynamic property for potential cancer treatment. *Smart Medicine* **2023**, *2*, e20230033, https://doi.org/10.1002/SMMD.20230033.
5. Ruoff, R.S.; Tse, D.S.; Malhotra, R.; Lorents, D.C. Solubility of fullerene (C60) in a variety of solvents. *J. Chem. Phys.* **1993**, *97*, 3379-3383, https://doi.org/10.1021/j100115a049.
6. Samoilova, N.A.; Krayukhina, M.A.; Klemenkova, Z.S.; Naumkin, A.V.; Buzin, M.I.; Mezhuev, Y.O.; Turetsky, E.A.; Andreev, S.M.; Anuchina, N.M.; Popov, D.A. Hydrophilization and Functionalization of Fullerene C_{60} with Maleic Acid Copolymers by Forming a Non-Covalent Complex. *Polymers* **2024**, *16*, 1736, https://doi.org/10.3390/polym16121736.
7. Huang, C.-W.; Chang, Y.-Y.; Cheng, C.-C.; Hung, M.-T.; Mohamed, M.G. Self-Assembled Supramolecular Micelles Based on Multiple Hydrogen Bonding Motifs for the Encapsulation and Release of Fullerene. *Polymers* **2022**, *14*, 4923, https://doi.org/10.3390/polym14224923.
8. Grodniski, D.C.; Benatto, L.; Gonçalves, J.P.; de Oliveira, C.C.; Pacheco, K.R.M.; Adad, L.B.; Coturi, V.M.; Roman, L.S.; Koehler, M. High photothermal conversion efficiency for semiconducting polymer/fullerene nanoparticles and its correlation with photoluminescence quenching. *Mater. Adv.* **2023**, *4*, 486-503, https://doi.org/10.1039/d2ma00912a.
9. Akhanova, N.Y.; Negim, E.-S.; Yerlanuly, Y.; Batryshev, D.G.; Eissa, M.M.; Schur, D.Y.; Ramazanov, T.S.; Al Azzam, K.M.; Muratov, M.M.; Gabdullin, M.T. Influence of fullerene content on the properties of polyurethane resins: A study of rheology and thermal characteristics. *Heliyon* **2024**, *10*, e33282, https://doi.org/10.1016/j.heliyon.2024.e33282.
10. Liu, S.-Y.; Wang, X.-R.; Li, M.-P.; Xu, W.-R.; Kuck, D. Water-soluble host–guest complexes between fullerenes and a sugar-functionalized tribenzotriquinacene assembling to microspheres. *Beilstein J. Org. Chem.* **2020**, *16*, 2551-2561, https://doi.org/10.3762/bjoc.16.207.

11. Aoshima, H.; Kokubo, K.E.N.; Shirakawa, S.; Ito, M.; Yamana, S.; Oshima, T. Antimicrobial Activity of Fullerenes and Their Hydroxylated Derivatives. *Biocontrol Sci.* **2009**, *14*, 69-72, https://doi.org/10.4265/bio.14.69.
12. Bolshakova, O.; Lebedev, V.; Mikhailova, E.; Zherebyateva, O.; Aznabaeva, L.; Burdakov, V.; Kulvelis, Y.; Yevlampieva, N.; Mironov, A.; Miroshnichenko, I.; *et al*. Fullerenes on a Nanodiamond Platform Demonstrate Antibacterial Activity with Low Cytotoxicity. *Pharmaceutics* **2023**, *15*, 1984, https://doi.org/10.3390/pharmaceutics15071984.
13. Borisenkova, A.A.; Bolshakova, O.I.; Titova, A.V.; Ryabokon, I.S.; Markova, M.A.; Lyutova, Z.B.; Sedov, V.P.; Varfolomeeva, E.Y.; Bakhmetyev, V.V.; Arutyunyan, A.V.; Burdakov, V.S.; Sarantseva, S.V. Fullerene C_{60} Conjugate with Folic Acid and Polyvinylpyrrolidone for Targeted Delivery to Tumor Cells. *Int. J. Mol. Sci.* **2024**, *25*, 5350, https://doi.org/10.3390/ijms25105350.
14. Mohanty, M.; Mohanty, P.S. Molecular docking in organic, inorganic, and hybrid systems: a tutorial review. *Monatsh. Chem.* **2023**, *154*, 683–707, https://doi.org/10.1007/s00706-023-03076-1.
15. Skariyachan, S.; Gopal, D.; Deshpande, D.; Joshi, A.; Uttarkar, A.; Niranjan, V. Carbon fullerene and nanotube are probable binders to multiple targets of SARS-CoV-2: Insights from computational modeling and molecular dynamic simulation studies. *Infect. Genet. Evol.* **2021**, *96*, 105155, https://doi.org/10.1016/j.meegid.2021.105155.
16. Chaudhary, M.; Tyagi, K. A REVIEW ON MOLECULAR DOCKING AND ITS APPLICATION. *Int. J. Adv. Res.* **2024**, *12*, 1141–1153, https://doi.org/10.21474/ijar01/18505.
17. Vogt, J.; Schulz, G.E. The structure of the outer membrane protein OmpX from *Escherichia coli* reveals possible mechanisms of virulence. *Structure* **1999**, *7*, 1301–1309, https://doi.org/10.1016/s0969-2126(00)80063-5.
18. Touw, D.S.; Patel, D.R.; van den Berg, B. The Crystal Structure of OprG from *Pseudomonas aeruginosa*, a Potential Channel for Transport of Hydrophobic Molecules across the Outer Membrane. *PLOS ONE* **2010**, *5*, e15016, https://doi.org/10.1371/journal.pone.0015016.
19. Jurado-Martín, I.; Sainz-Mejías, M.; McClean, S. *Pseudomonas aeruginosa*: An Audacious Pathogen with an Adaptable Arsenal of Virulence Factors. *Int. J. Mol. Sci.* **2021**, *22*, 3128, https://doi.org/10.3390/ijms22063128.
20. Duggan, S.; Laabei, M.; Alnahari Alaa, A.; O'Brien Eóin, C.; Lacey Keenan, A.; Bacon, L.; Heesom, K.; Fu, C.-L.; Otto, M.; Skaar, E.; McLoughlin Rachel, M.; Massey Ruth, C. A Small Membrane Stabilizing Protein Critical to the Pathogenicity of *Staphylococcus aureus*. *Infect. Immun.* **2020**, *88*, https://doi.org/10.1128/iai.00162-20.
21. N-methyl-2-pyrrolidone. Available online: https://pubchem.ncbi.nlm.nih.gov/compound/N-methyl-2-pyrrolidone (**16.09.2004)**.
22. Chavez-Esquivel, G.; Cervantes-Cuevas, H.; Ybieta-Olvera, L.F.; Castañeda Briones, M.T.; Acosta, D.; Cabello, J. Antimicrobial activity of graphite oxide doped with silver against *Bacillus subtilis*, *Candida albicans*, *Escherichia coli*, and *Staphylococcus aureus* by agar well diffusion test: Synthesis and characterization. *Mater. Sci. Eng. C* **2021**, *123*, 111934, https://doi.org/10.1016/j.msec.2021.111934.
23. Berman, H.M.; Burley, S.K. Protein Data Bank (PDB): Fifty-three years young and having a transformative impact on science and society. *Quart. Rev. Biophys.* ***2025***, *58*, *e9*, https://doi.org/10.1017/S0033583525000034.
24. Burley, S.K.; Piehl, D.W.; Vallat, B.; Zardecki, C. RCSB Protein Data Bank: supporting research and education worldwide through explorations of experimentally determined and computationally predicted atomic level 3D biostructures. *IUCrJ* **2024**, *11*, 279–286, https://doi.org/10.1107/S2052252524002604.
25. Rosignoli, S.; Lustrino, E.; Di Silverio, I.; Paiardini, A. Making Use of Averaging Methods in MODELLER for Protein Structure Prediction. *Int. J. Mol. Sci.* **2024**, *25*, 1731, https://doi.org/10.3390/ijms25031731.
26. Webb, B.; Sali, A. Comparative Protein Structure Modeling Using MODELLER. *Curr. Protoc. Bioinform.* **2016**, *54*, 5.6.1-5.6.37, https://doi.org/10.1002/cpbi.3.
27. Linhares, M.; Kelry Costa Guimarães, D.; Santos, K.V.Z.d.; Barros, H.L.d.; Miranda, M.R.; Silva, K.A.d. Ramachandran Chart: Validating Proteins Through a Three- Dimensional Structure. *Int. J. Innov. Educ. Res.* **2022**, *10*, 61-68, https://doi.org/10.31686/ijier.vol10.iss12.3971.
28. Cammisa, M.; Correra, A.; Andreotti, G.; Cubellis, M.V. Identification and analysis of conserved pockets on protein surfaces. *BMC Bioinformatics* **2013**, *14*, S9, https://doi.org/10.1186/1471-2105-14-S7-S9.
29. Prymula, K.; Jadczyk, T.; Roterman, I. Catalytic residues in hydrolases: analysis of methods designed for ligand-binding site prediction. *J. Comput. Aided Mol. Des.* **2011**, *25*, 117-133,

https://doi.org/10.1007/s10822-010-9402-0.
30. Bhachoo, J.; Beuming, T. Investigating Protein–Peptide Interactions Using the Schrödinger Computational Suite. In Modeling Peptide-Protein Interactions: Methods and Protocols, Schueler-Furman, O., London, N., Eds.; Springer New York: New York, NY, **2017**; Volume 1561, pp. 235-254, https://doi.org/10.1007/978-1-4939-6798-8_14.
31. Liebschner, D.; Moriarty, N.W.; Poon, B.K.; Adams, P.D. *In situ* ligand restraints from quantum-mechanical methods. *Acta Crystallogr. D* **2023**, *79*, 100-110, https://doi.org/10.1107/S2059798323000025.
32. Kim, S.; Chen, J.; Cheng, T.; Gindulyte, A.; He, J.; He, S.; Li, Q.; Shoemaker, B.A.; Thiessen, P.A.; Yu, B.; Zaslavsky, L.; Zhang, J.; Bolton, E.E. PubChem 2025 update. *Nucleic Acids Res.* **2025**, *53*, D1516-D1525, https://doi.org/10.1093/nar/gkae1059.
33. Forli, S.; Huey, R.; Pique, M.E.; Sanner, M.F.; Goodsell, D.S.; Olson, A.J. Computational protein–ligand docking and virtual drug screening with the AutoDock suite. *Nat. Protoc.* **2016**, *11*, 905-919, https://doi.org/10.1038/nprot.2016.051.
34. Geidl, S.; Bouchal, T.; Raček, T.; Svobodová Vařeková, R.; Hejret, V.; Křenek, A.; Abagyan, R.; Koča, J. High-quality and universal empirical atomic charges for chemoinformatics applications. *J. Cheminform.* **2015**, *7*, 59, https://doi.org/10.1186/s13321-015-0107-1.
35. Khan, F.; Bafna, S.; Gupta, T.; Isaac, A.E. Virtual Screening of potential inhibitors from Herbs for the treatment of Breast Cancer. *Asian J. Pharm. Clin. Res.* **2017**, *10*, 62-67, https://doi.org/10.22159/ajpcr.2017.v10i4.14959.
36. Aguiar, C.; Camps, I. Molecular Docking in Drug Discovery: Techniques, Applications, and Advancements. *Curr. Med. Chem.* **2025**, *32*, 5924–5938, https://doi.org/10.2174/0109298673325827240926081845.
37. Buckley, M.E.; Ndukwe, A.R.N.; Nair, P.C.; Rana, S.; Fairfull-Smith, K.E.; Gandhi, N.S. Comparative Assessment of Docking Programs for Docking and Virtual Screening of Ribosomal Oxazolidinone Antibacterial Agents. *Antibiotics* **2023**, *12*, 463, https://doi.org/10.3390/antibiotics12030463.
38. Carbone, J.; Ghidini, A.; Romano, A.; Gentilucci, L.; Musiani, F. PacDOCK: A Web Server for Positional Distance-Based and Interaction-Based Analysis of Docking Results. *Molecules* **2022**, *27*, 6884, https://doi.org/10.3390/molecules27206884.
39. Zajaček, D.; Dunárová, A.; Bucinsky, L.; Štekláč, M. Compromise in Docking Power of Liganded Crystal Structures of M^{pro} SARS-CoV-2 Surpasses 90% Success Rate. *J. Chem. Inf. Model.* **2024**, *64*, 1628-1643, https://doi.org/10.1021/acs.jcim.3c01552.
40. Meng, E.C.; Goddard, T.D.; Pettersen, E.F.; Couch, G.S.; Pearson, Z.J.; Morris, J.H.; Ferrin, T.E. UCSF ChimeraX: Tools for structure building and analysis. *Protein Sci.* **2023**, *32*, e4792, https://doi.org/10.1002/pro.4792.
41. Pettersen, E.F.; Goddard, T.D.; Huang, C.C.; Meng, E.C.; Couch, G.S.; Croll, T.I.; Morris, J.H.; Ferrin, T.E. UCSF ChimeraX: Structure visualization for researchers, educators, and developers. *Protein Sci.* **2021**, *30*, 70-82, https://doi.org/10.1002/pro.3943.
42. Belanger, C.R.; Hancock, R.E.W. Testing physiologically relevant conditions in minimal inhibitory concentration assays. *Nat. Protoc.* **2021**, *16*, 3761-3774, https://doi.org/10.1038/s41596-021-00572-8.
43. Kadeřábková, N.; Mahmood, A.J.S.; Mavridou, D.A.I. Antibiotic susceptibility testing using minimum inhibitory concentration (MIC) assays. *npj Antimicrob. Resist.* **2024**, *2*, 37, https://doi.org/10.1038/s44259-024-00051-6.
44. Owuama, C.I. Determination of minimum inhibitory concentration (MIC) and minimum bactericidal concentration (MBC) using a novel dilution tube method. *Afr. J. Microbiol. Res.* **2017**, *11*, 977-980, https://doi.org/10.5897/AJMR2017.8545.
45. Elhosiny Ali, H.; Algarni, H.; Yahia, I.S.; Khairy, Y. Optical absorption and linear/nonlinear parameters of polyvinyl alcohol films doped by fullerene. *Chin. J. Phys.* **2021**, *72*, 270-285, https://doi.org/10.1016/j.cjph.2021.04.022.
46. Kamnev, A.A.; Dyatlova, Y.A.; Kenzhegulov, O.A.; Vladimirova, A.A.; Mamchenkova, P.V.; Tugarova, A.V. Fourier Transform Infrared (FTIR) Spectroscopic Analyses of Microbiological Samples and Biogenic Selenium Nanoparticles of Microbial Origin: Sample Preparation Effects. *Molecules* **2021**, *26*, 1146, https://doi.org/10.3390/molecules26041146.
47. Behera, M.; Ram, S. Mechanism of Solubilizing Fullerene C_{60} in Presence of Poly(Vinyl pyrrolidone) Molecules in Water. *Fullerenes, Nanotubes Carbon Nanostruct.* **2015**, *23*, 906–916, https://doi.org/10.1080/1536383X.2015.1041109.

48. Tong, J.; Zimmerman, M.C.; Li, S.; Yi, X.; Luxenhofer, R.; Jordan, R.; Kabanov, A.V. Neuronal uptake and intracellular superoxide scavenging of a fullerene (C_{60})-poly(2-oxazoline)s nanoformulation. *Biomaterials* **2011**, *32*, 3654-3665, https://doi.org/10.1016/j.biomaterials.2011.01.068.
49. Eom, T.; Barát, V.; Khan, A.; Stuparu, M.C. Aggregation-free and high stability core–shell polymer nanoparticles with high fullerene loading capacity, variable fullerene type, and compatibility towards biological conditions. *Chem. Sci.* **2021**, *12*, 4949-4957, https://doi.org/10.1039/d1sc00602a.
50. Wilhelm, M.J.; Sharifian Gh, M.; Wu, T.; Li, Y.; Chang, C.-M.; Ma, J.; Dai, H.-L. Determination of bacterial surface charge density via saturation of adsorbed ions. *Biophys. J.* **2021**, *120*, 2461-2470, https://doi.org/10.1016/j.bpj.2021.04.018.
51. Sobolev, O.V.; Afonine, P.V.; Moriarty, N.W.; Hekkelman, M.L.; Joosten, R.P.; Perrakis, A.; Adams, P.D. A Global Ramachandran Score Identifies Protein Structures with Unlikely Stereochemistry. *Structure* **2020**, *28*, 1249-1258.e1242, https://doi.org/10.1016/j.str.2020.08.005.
52. Shenoy, V.; Gunda, R.; Noble, C.; Haraguchi, A.; Stevenson, S.; Daniel, J. Fullertubes inhibit mycobacterial viability and prevent biofilm formation by disrupting the cell wall. *Cell Biochem. Funct.* **2024**, *42*, e3963, https://doi.org/10.1002/cbf.3963.
53. Xie, W.; Zhang, S.; Pan, F.; Chen, S.; Zhong, L.; Wang, J.; Pei, X. Nanomaterial-based ROS-mediated strategies for combating bacteria and biofilms. *J. Mater. Res.* **2021**, *36*, 822-845, https://doi.org/10.1557/s43578-021-00134-4.

Publisher's Note & Disclaimer